Fluorine-19 MRI Contrast Agents for Cell Tracking and Lung Imaging

Supplementary Issue: New Concepts in Magnetic Resonance as Applied to Cellular and In Vivo Applications

Matthew S. Fox[1,2], Jeffrey M. Gaudet[1,2] and Paula J. Foster[1,2]

[1]Department of Medical Biophysics, University of Western Ontario, London, ON, Canada. [2]Imaging Research Laboratories, Robarts Research Institute, London, ON, Canada.

ABSTRACT: Fluorine-19 (^{19}F)-based contrast agents for magnetic resonance imaging stand to revolutionize imaging-based research and clinical trials in several fields of medical intervention. First, their use in characterizing in vivo cell behavior may help bring cellular therapy closer to clinical acceptance. Second, their use in lung imaging provides novel noninvasive interrogation of the ventilated airspaces without the need for complicated, hard-to-distribute hardware. This article reviews the current state of ^{19}F-based cell tracking and lung imaging using magnetic resonance imaging and describes the link between the methods across these fields and how they may mutually benefit from solutions to mutual problems encountered when imaging ^{19}F-containing compounds, as well as hardware and software advancements.

KEYWORDS: fluorine-19, cellular therapy, cell tracking, lung imaging, MRI, isoflurane

**CORRESPONDENCE:** matthew.s.fox.4@gmail.com

Introduction

Fluorine-19 (^{19}F) has the potential to revolutionize imaging-based cell tracking, lung imaging, and drug development by enabling alternate routes for clinical translation of these techniques to patients. ^{19}F is a versatile and nuclear magnetic resonance (NMR) active nucleus. Observations were originally attempted in 1942 using NMR[1] and later with magnetic resonance imaging (MRI) in the 1970s,[2] when numerous applications were surmised. ^{19}F T_1 relaxation rates were first used in the early 1990s to determine the intracellular partial pressure of oxygen, but direct fluorine imaging still proved elusive.[3] Technology has caught up with the predictions of the past and MRI contrast agents containing ^{19}F are now at the forefront of imaging research in a variety of biomedical fields such as cell tracking, lung imaging and drug development. Figure 1 clearly demonstrates an increase in the number of publications for ^{19}F-based MRI cell tracking within the past decade. From an MRI point of view, ^{19}F is part of the family of nonproton nuclei (or X-nuclei). It is 100% naturally abundant and has a spin of 1/2, a gyromagnetic ratio of appreciable size (94%, the largest of X-nuclei) compared with protons (^{1}H), and sensitivity of 83% relative to ^{1}H. Commonly used fluorinated contrast agents that are used to probe the microbiological and macrobiological environments include perfluorocarbons (PFCs) such as perfluoropolyether (PFPE), perfluoro-15-crown-5-ether (PFCE), sulfur hexafluoride (SF_6), perfluoropropane (C_3F_8), and hexafluoroethane (C_2F_6). Their usage and important physical properties are conveniently summarized in Table 1. Fluorinated contrast agents are used to probe the microbiological environment as cell-labelling agents[4] and theranostic drugs and therapies. Therapeutic delivery of labeled cells using PFC emulsions (eg, dendritic cells [DCs][4]) or drugs (eg, 5-fluorouracil[5]) containing ^{19}F can be quantified and tracked noninvasively and longitudinally using MRI. Agents such as fluorinated gases are also useful for probing macrobiological environments such as the airspaces of lungs.[6] Inert fluorinated gases containing multiple chemically equivalent ^{19}F atoms per molecule are used in the field of MRI of the lung as inhaled contrast agents to probe lung structure and function noninvasively. This article discusses the role of ^{19}F in the fields of cell tracking and lung imaging. Many new contributions have been reported in the past few years in these fields and their importance will be discussed. Though drug development is a large contributor to the ^{19}F body of literature, its scope is vast, and we direct interested readers to the thorough review on the role of ^{19}F in imaging and drug development by Bartusik and Aebisher.[7]

Cell Tracking Using Imaging Techniques

Cell tracking is an important tool for the field of cellular therapy. The goals of cellular therapy are to stimulate the immune
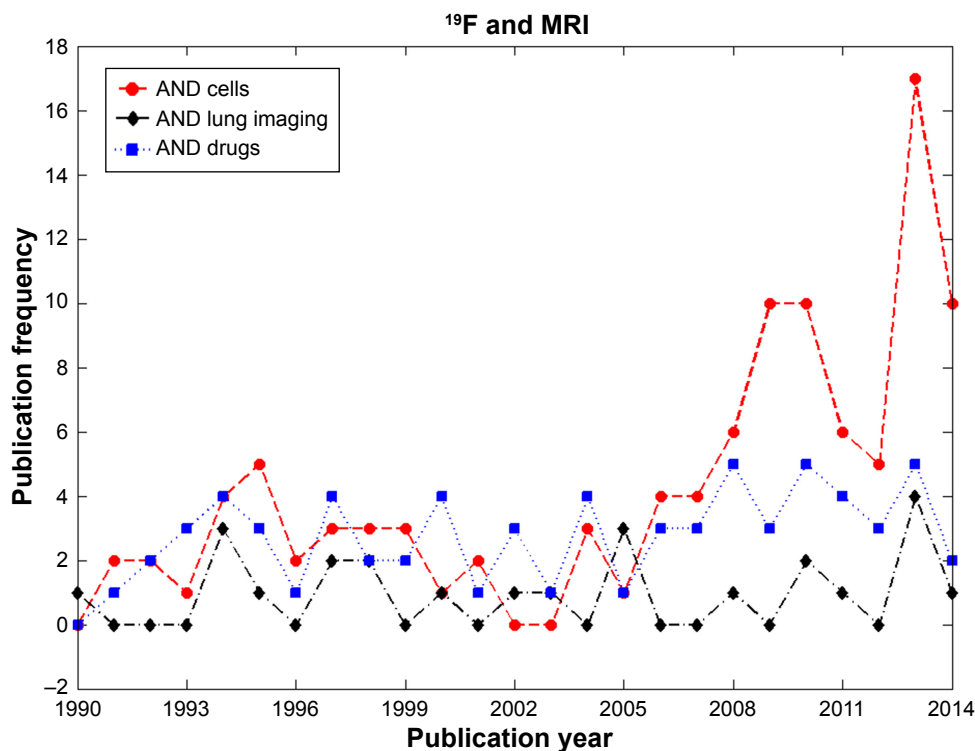
Figure 1. Publication frequency by year for "^{19}F and MRI" on PubMed. Additional search parameters are included in the legend separating out the fields of cell tracking, lung imaging, and drug development. The rate of publications for ^{19}F-based cell tracking is observed to increase over the past decade since the initial demonstration of the concept in 2005.[4]

system to elicit an immune response, eg, in cancer patients, and regenerate damaged tissues using stem cells. The requirement and need to track cells noninvasively is of great importance for the development of cellular therapies and vaccines for eventual clinical translation and acceptance. Therefore, cell tracking is a necessary tool in order to help answer the questions: How many cells were actually transplanted? How long do transplanted cells survive? Do transplanted cells migrate and reach their therapeutic targets? Though theory can help predict the status of cells and routes of migration, in practice, the outcomes are often very different and patient specific, which is why methods of noninvasive imaging are needed. Previously developed cell-tracking techniques employed the use of fluorescent labels, radio labels, iron labels, and combinations of these for dual-mode identification (eg, iron with fluorescent tags), but all of these techniques have restrictions on clinical feasibility, which will be described in the following sections. Fluorinated contrast agents have emerged as a recent addition to these techniques in the form of PFC emulsions and other fluorinated compounds.

It is important for any cell-labelling strategy that the substances used as labelling agents do not alter the properties of cells, do not cause cytotoxic effects to the cells, and do not change their phenotype or behavior. Using fluorescence-activated cell sorting (FACS), consistency of cell phenotype can be verified aiding in a novel label development. Simple assays using trypan blue can be used to compare cell viability with and without label to reveal any negative cytotoxic effects of the label on therapeutic cells. Practical issues arising from cell label retention are cell division, cell death, and the potential for bystander cells to adopt labels. Cell division leads to a dilution of contrast agent content per cell, reducing their individual detectability for highly localized labeled cells. Upon cell death, the label is free to leak out from the cells and become dispersed. Bystander cells may phagocytose the recently released label from dead cells and contribute to false-positive results. Important clinical translation considerations include the safety profile of the labelling agents, whether there are any toxic effects, and how the labels are metabolized and cleared from the body (biological half-life) once they leave the cells they initially resided in.

Nonfluorinated Cell-Tracking Methods

Previously developed cell-tracking methods include the use of fluorescence microscopy, positron emission tomography (PET) using radioactive agents to label cells, and MRI using heavy metal contrast agents (eg, superparamagnetic iron oxide [SPIO], Gd). Fluorescence microscopy using fluorescently tagged cells has the ability to reveal tagged cells in organs with enough resolution and signal-to-noise ratio (SNR) to resolve even single cells. However, the ability to observe cells in vivo using these methods becomes difficult as tissue depth increases, limiting in vivo studies to small animals. A thorough review of fluorescence molecular imaging can be found here.[8]

Table 1. Properties of common ^{19}F substances used in the fields of cell tracking and lung imaging. Numbers of equivalent atoms (strongest peak) are presented as well as various reported relaxation times and the corresponding field strengths for each substance. Citations are superscripted and known special conditions are subscripted.

	USED IN	SINGLE PEAK	#^{19}F SPINS	T_1 (ms)	T_2 (ms)	T_2* (ms)
PFPE	Cell tracking	No	28–36[56]	3T 470[57] / 7T 590[56]ae 425[32]d / 9.4T 510[56]ae / 11.7T 437[53,38] 280[33]e 380[33]c / 14.1T 400[56]ae	3T 250[57] / 7T 82[32]d / 11.7T 153[33]e 68[33]c	<10 ms[51]f
PFCE	Cell tracking	Yes	20[56]	7T 2500[56]ae 950[41]c / 9.4T 580[43] 600[31]d 1000[79]c 1180[31]e 1350[89]h 1400[89]g 1670[56]ae / 11.7T 800[58]c / 14.1T 1120[56]ae	7T 50[41]c / 9.4T 25[89]h 300[31]e 350[79]c 440[89]g 536[43]g 525[31]d	
SF$_6$	Lung imaging, ultrasound	Yes	6	1.5T 1.2[114] / 3T 1.2[109]b 2[124]b		3T 1[124]b / 4.7T 2.7[116]b
C$_2$F$_6$	Lung imaging	Yes	6	1.9T 5.9[108]b	1.9T 5.3[108]b	
C$_3$F$_8$	Lung imaging	No	6	1.5T 18[113] / 3T 12.4[109]b	1.5T 16[113]	3T 2.2[109]b 10[124]b

Notes: aExtrapolated from data at 310K (Kadayakara et al.)[56]; bin vivo; cinternalized within cells; demulsion; eneat; ffield not reported; gsaline, hblood.

The use of radio labels in single-photon emission computed tomography (SPECT) and PET provides high sensitivity and has been used for cell-tracking applications.[9–11] There are some significant drawbacks to these techniques, which include the following: their radioactive nature, which imparts ionizing radiation to cells and tissues, resulting in potential cytotoxicity to the cells they label; relatively short nuclear half-lives, limiting the effectiveness for longitudinal studies; and limited spatial resolution. However, the latter may be overcome by recent developments in modern combined MR/PET or PET/computed tomography (CT) systems to provide improved localization of cells due to high-resolution anatomical imaging from their MR and CT counterparts.

Cell tracking using iron labels was first utilized by Bulte et al and Yeh et al in the early 1990s by internalizing dextran-coated magnetite particles and SPIO particles (Aquamag100 and BMS 180549) within cells and detecting them using MRI.[12–14] Iron-labeled cells are usually identified by the negative contrast observed in MR images due to their enhancement of R_2 and R_2*, though positive contrast methods also exist using methods such as ultrashort echo time (UTE)[15] imaging and sweep imaging with Fourier transformation.[16] These regions of signal voids are of much larger spatial extent than the cells themselves due to local changes in magnetic susceptibility. Small quantities of label can have large detectable effects on the magnetization of surrounding protons making their regional detection easy using MRI. Later developments in methods and technology lead to the ability to detect single cells labeled with iron in vivo using MRI as demonstrated by Heyn et al and Shapiro et al.[17,18]

Though iron labelling is a powerful tool for longitudinal cell tracking using MRI, quantification of absolute cell numbers is difficult since the correlation between void volume and iron concentration is only linear for small concentrations of internalized iron.[19] Furthermore, it can be difficult to discern negative contrast generated by iron with those from natural effects or image artifacts. Several reviews have been published in recent years describing technological and methodological advancements as well as the future of cell tracking using SPIO and ^{19}F-labeled cells.[20–23]

Fluorinated Contrast Agents for Cell Tracking Using MRI

The use of PFCs for cell tracking using MRI was first demonstrated in 2005 by Ahrens et al describing a complete imaging platform for tracking immunotherapeutic cells.[4] PFC-labeled cells provide direct detection of cells in the form of positive-contrast *hot-spot* density-weighted images[24] owing to the inherent lack of ^{19}F background signal in vivo. Furthermore, unlike iron, the use of ^{19}F labels do not distort the local magnetic field enabling the ability to collect complementary high-resolution images of the underlying anatomical structures using ^{1}H MRI. After registration of images obtained using both nuclei, these images aid in the verification and localization of labeled cells within injection sites or those that have migrated to organs or lymph nodes. Another advantage over iron is that the PFCs detectable signal is directly proportional to the amount of internalized PFC within each cell, enabling quantitative cell tracking.

Labelling of cells using PFCs can be performed using ex vivo methods (cell culture flasks) or in situ as an injection (usually intravenous). For the ex vivo case, cells are incubated at a specific concentration of cells (typically 2×10^5 cells/mL) and ^{19}F-containing label within the cell media in order to promote cellular uptake. Uptake is not instantaneous, and there is an optimum label dose and incubation time depending on the agent used and due to natural cell division during the labelling period. Potential cytotoxic effects can occur due to extended exposure to high concentrations of label within the media. This is further complicated by the fact that these optima are different for each cell type of interest. These parameters are important to map out to maximize the cellular uptake of label (which translates to improved SNR within post transplant images) as well as to ensure that the labels do not affect the cells' behavior (eg, migration, differentiation, and surface marker expression). One method to increase the available SNR within the cells is to increase the number of ^{19}F spins by means of using larger label particle sizes. However, it has been shown that there is an optimum size where smaller sized particles (<560 nm) do not disrupt cell behavior.[25] Labelling cells ex vivo is a very powerful technique owing to the ability to label specific cells in controlled conditions with the potential to quantify absolute counts of cells.

Cell labelling in situ is more straightforward but less target specific and lacks the potential to quantify cell numbers absolutely. To label cells in situ, an injectable PFC emulsion is formulated and administered intravenously. While within the vascular system, circulating cells (monocytes, macrophages, etc.) phagocytose the label and become PFC-labeled cells. Cells labeled this way usually consist of a distribution of cell types possessing variable label concentration. This technique is often used to label the influx of inflammatory macrophages responding to a recent insult.[26–31]

Noncommercial and Commercial Agents for Cell Tracking

There are a variety of commercial and noncommercial fluorinated labelling agents currently available for use for cell labelling. These include linear PFCs such as the PFPE Cell Sense (CS-1000, CS-1000 ATM and fluorescently tagged CS-ATM DM Red, Green, NIR),[32–38] V-Sense (VS-1000H),[27,39,40] and cyclic PFCs such as PFCE-based agents,[29,41–44] including VS-580H, which is a commercial PFCE,[45–47] as well as other PFC formulations such as perfluorooctyl bromide (PFOB),[31] perfluorodecalin (PFD),[31] trans-bis-perfluorobutyl ethylene (F-44E),[31] and superfluorinated compounds (eg, PERFECTA[48] and [19]FIT.[49]) These latter formulations aim to provide more SNR per cell (by fitting even more ^{19}F atoms per molecule within the labels while maintaining small particle sizes) and adding additional functionality such as the ability to cleave the molecule apart for easy clearance by enzymatic action.[48,50] Additional information on the hydrodynamic diameter and specific target of many PFC agents has been well summarized in previous reviews.[51]

At the time of writing this article, Cell Sense and V-Sense are the two commercially available PFCs used for cell tracking in MRI, which are manufactured by Celsense Inc. They have developed several formulations of ex vivo and in situ cell labels, which were originally filed for patent on May 2, 2008 (no. PCT/US2009/002706). These include fluorinated emulsions (CS-1000, CS-580, VS-1000H, VS-580H) as well as other formulations that incorporate fluorochromes (CS and VS—ATM DM Red, Green, and NIR) for detection with MRI and fluorescence microscopy (ie, dual-labeled cells). Formulations using the numerical suffix "1000" are composed using PFPE, whereas those using "580" are composed from PFCE. To our knowledge, this company manufactures the only Food and Drug Administration-approved PFC label suitable for clinical cell tracking (ie, CS-1000) providing groundwork and a desirable research route for translational cell tracking and cellular therapy clinical trials. The safety of some PFCs in biomedical applications has been investigated previously. The PFC PFOB has been characterized and used as a blood substitute in large quantities.[24,52] The amounts of PFC used as in situ and ex vivo agents for cell tracking are quite small in comparison with the quantities used as blood substitutes. This reduces the concern of residual

label and clearance over time. Clearance of PFC from the body is primarily achieved via the reticuloendothelial system and the lungs.[52]

Cell Quantification from Imaging

The ability to quantify the MRI signal obtained from ^{19}F images of PFC-labeled cells is paramount to the development of future cellular therapies leading to conclusions about cell fate after administration. Ex vivo techniques allow for the quantification and potential to measure absolute cell counting from MR images. The processes involved are depicted in Figure 2 and are as follows. Cells are first labeled by incubating them with a ^{19}F-based labelling agent (typically 48 hours). Three important measurements are required for quantification: The fractional PFC content per cell, denoted Fc, the SNR obtained from a uniform reference phantom (typically a dilution of the original cell labelling agent), and the SNR obtained from the regions of interest containing the cells themselves. Obtaining Fc is an extra step using a small fraction of the labeled cells separated from the transplant batch, as shown in process 1. To calculate Fc, this known quantity of cells is characterized using NMR and its spectrum is compared with a reference possessing a known concentration of ^{19}F within the same NMR tube (trifluoroacetic acid [TFA]). Process 2 involves obtaining conventional ^{1}H MR images in animal models or human beings

after the injection of ^{19}F-labeled cells to obtain the underlying anatomy at high resolution. Finally, in process 3, ^{19}F MRI is performed depicting ^{19}F signal from the reference phantom as well as the injected labeled cells. Obtaining the SNR values from injected cells and the reference phantom within these images, together with Fc, enable the estimation of the number of cells detected within an image. These methods are described in detail by Srinivas et al.[53] Numerous in vitro quantification studies using this method have reported a Pearson correlation coefficient (R^2) of >0.95 between the observed number of cells and the true number of cells demonstrating accuracy and repeatability.[53–55] Celsense Inc. has developed a postprocessing tool called Voxel Tracker[34,53] for use with the company's contrast agents, though this software may be suitable in principle for quantifying any cells labeled using ^{19}F-containing agents (commercial or not). Other softwares commonly used for quantifying labeled cells include ImageJ and MATLAB, which offer more flexibility in postprocessing choices. Quantification of signal from in situ labeled cells also relies on the use of a uniform reference phantom, producing uniform signals within the image where, for example, inflammation correlates are to be quantified. Because the relationship between SNR and PFC content within each voxel is linear, it is easy to derive a correlation between the amount of SNR produced by labeled cells with that of known reference. From this,
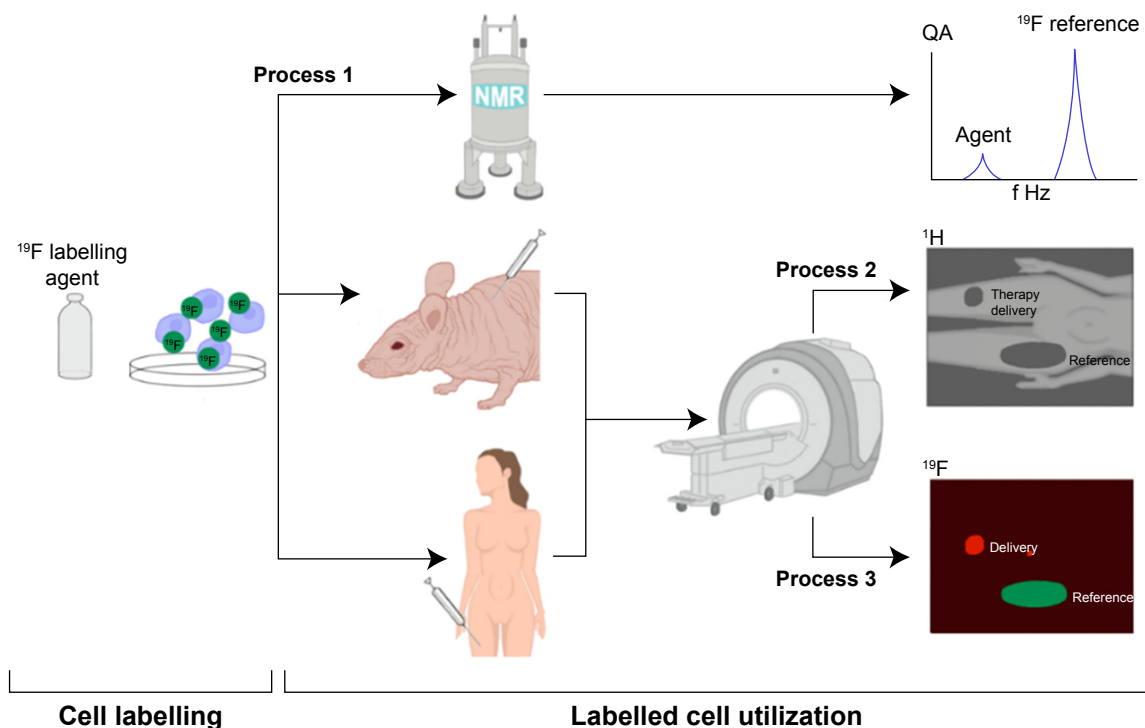
Figure 2. This figure depicts the ex vivo labelling process for absolute labeled cell quantification. During the cell-labelling phase, cells are first incubated with a ^{19}F-based agent for up to 48 hours in order for ^{19}F spins to become internalized within cells. Labeled cells are then utilized in three different processes. Process 1 demonstrates the performing of NMR on a small sample of these labeled cells to obtain their fractional fluorine content (Fc). Process 2 involves conventional ^{1}H imaging of animals and human beings post injection to provide the underlying anatomy. Process 3 involves ^{19}F imaging of animals and human beings to provide signals from both a reference phantom of known concentration and signals from the injected cells. The signals from these images, combined with Fc, allow for quantification of injected cells.

a reliable inflammation index can be generated by quantifying the SNR obtained from different organs within the region of interest.[26] Unfortunately, estimation of the number of inflammatory cells is currently not possible due to the inability to measure Fc for this mode of labelling.

Physical Properties, Hardware, Pulse Sequences, and Reconstruction

In addition to the various labelling agents available, raw numbers of ^{19}F per molecule, relative chemical shifts, MRI hardware, and pulse sequence development play an important role in increasing the sensitivity and detectability of PFC-labeled cells.

Important physical properties of commonly used PFCs are their spin–lattice (T_1) and spin–spin (T_2) relaxation rates, chemical shift properties, and spectral strength (number of equivalent ^{19}F atoms). Table 1 summarizes many of these properties for PFPE- and PFCE-based labelling agents. Identification of resonant frequencies of novel PFCs is achieved by comparing to reference samples containing known quantities of ^{19}F atoms. Typical references include trichlorofluoromethane (TFE) and the more commonly reported reference, TFA. Different PFCs possess different chemical shift values, mono or multispectral features, and different relaxation times. PFPE and PFCE are separated by 1.9 ppm when measured independently, relative to $CFCl_3$ (another reported reference chemical).[56] PFPE has a spectrum characterized by two distinct peaks separated by 0.2 ppm.[56] The primary peak is 10 times stronger than the secondary peak and has a chemical shift of −15.58 ppm relative to TFA.[34] The second peak is generally not observed in vivo due to its signal strength being an order of magnitude smaller than the main peak and its shorter relaxation time. The T_1 of the primary peak is 2.2 times shorter than that of PFCE with a value of 437 ms at 11.7 T.[38,53] Boehm-Sturm et al reported T_1/T_2 of both free and cell-internalized PFPE of 280/153 ms and 380/68 ms, respectively, also at 11.7 T.[33] Ahrens et al reports T_1/T_2 values of 470/250 ms for PFPE at the clinically relevant field strength 3 T.[57] In contrast to PFPE, PFCE has the benefit of exhibiting a single strong peak owing to its circular symmetry. Longitudinal relaxation times are longer for PFCE, which is why some users prefer PFPE. Intracellular T_1 of a particular PFCE has been reported to be 800 ms at 11.7 T.[58] Ruiz-Cabello et al investigated cationic PFCE at 9.4 T and reported T_1/T_2 values of 580 ms/536 ms,[43] and Jacoby et al reported T_1/T_2 values of 600 ms/300 ms using a different emulsion formulation of PFCE.[31] They include a table of relaxation times for the complicated spectra of PFOB, PFCE, PFD, and F44E. A thorough investigation of the relaxation of PFPE and PFCE in neat and emulsion forms was conducted recently by Kadayakkara et al investigating neat and emulsified samples at different field strengths (7–14.1 T) and for a range of different temperatures (256K–323K).[56] Important reported trends include that for PFCE, R_1 ($R_1 = 1/T_1$) decreased as a function of temperature for each of the three

different field strengths and R_1 increased as a function of field strength. Emulsions exhibited a reduction in R_1 by 20% compared with neat samples. PFPE exhibited an increase in R_1 as a function of field strength and as a function of temperature but reached a maximum R_1 value at a specific temperature that was different for each field strength. Knowledge of these trends will help improve the development of customized PFC cell-tracking probes at clinical field strengths and for eventual clinical translation.

Research utilizing PFCs for cell tracking requires additional hardware not available on all scanners. Broadband amplifiers capable of nonproton excitation are generally required as are dedicated radiofrequency (RF) coils capable of detecting the ^{19}F resonance. The separation between ^1H and ^{19}F frequencies is small compared with that of other nuclei (~4–30 kHz between 1.5 and 11.7 T). For clinical field strengths, existing amplifiers may be sufficient for the detection of ^{19}F signals without the need for an expensive multinuclear package. RF coils capable of detecting both ^1H and ^{19}F signals are desirable for both preclinical and clinical imaging. Some examples include single-tuned linear coils and dual-tuned coils that can be manually or electronically switched between scans.[57] A big advantage of dual-tuned coils is that switching between ^1H and ^{19}F modes can be performed without having to remove the sample, animal, or patient from the bore.[54]

Together with these specialized RF coils, MRI pulse sequences are needed. The majority of reported work using PFCs for MRI cell tracking utilized fast spin-echo pulse sequences such as rapid acquisition with relaxation enhancement.[4,27–29,32,33,40,42,43,45,46,59,60] Due to the refocusing pulse, this sequence has the advantage of decreasing T_2^* effects, which can complicate quantification. In addition, fast spin-echo is a common and familiar sequence that is widely available on most MRI systems. Recent interest in other pulse sequences that utilize SNR per unit time (SNR/t) more efficiently include the use of balanced steady-state free precession[37,58,61] and UTE imaging.[62] These sequences are capable of improving SNR by either averaging hundreds of times or minimizing signal dephasing. Another advantage comes from the short echo times (TEs) utilized by both of these sequences, which result in spin-density weighted images allowing for quantification. The improvement in imaging speed comes at a cost requiring higher gradient performance. A multispin echo sequence has also been developed[63] suitable for possible future cell-tracking applications using PFOB. It is interesting to note that the initial investigation into imaging ^{19}F agents utilized steady-state free precession techniques as early as 1977.[2]

Image reconstruction considerations are important as well. Detecting small populations of PFC-labeled cells does not yield exceedingly high SNR values (~5–15), and SNR thresholds (to distinguish real signal from background) are typically quite low (between 2.5 and 5). Postprocessing is required for low SNR data by performing Rician noise corrections[53,64] and for removing artifacts caused by chemical

shifts.[65] Compressed sensing is an imaging method that uses sophisticated image reconstruction to form images from sparsely filled k-space data, with the advantage of significant shortening of scan time.[66–68] Patient motion can further impact image quality and reduce SNR, which has implications on absolute cell quantification.[69]

Applications of PFC to Cell Tracking

Since 2005, PFC cell tracking has been applied to numerous cell types and disease models, including the tracking of endothelial cells,[55] inflammation (macrophages),[26–29,31,42,45,47,59,70–73] monocytes,[30,39,74] cancer cells,[75–78] human-derived mesenchymal stem cells (hMSCs),[36,37,61] stem/progenitor cells,[58] DCs,[4,25,34,41,44,79,80] T-cells,[38,53,78,81] hematopoietic stem cells,[35] neural stem cells,[32,33,43] and natural killer cells.[82]

Mesenchymal stem cells (MSCs) are of recent interest in cellular therapy due to their ability to modulate various immune responses[83] and their capability of differentiating into various tissues such as bone, cartilage, and adipose.[84] Not surprisingly, PFC cell tracking has been recently used to investigate mouse-derived MSC (mMSC) and hMSC.[36,37,61] The development of hardware and imaging protocols in these animal models is essential to lay the groundwork for future clinical translation.[36,37,61] A recent study investigated the fate of MSC implants labeled using CS-1000 in two mouse transplant models using immunocompetent and immunocompromised mice.[61] mMSC (2×10^6) and hMSC (1.5×10^6) were delivered to competent and compromised mice, respectively, and were imaged at four time points for up to 17 days. For both mice, day zero quantification agreed well with the expected implanted cell numbers. Over time, ^{19}F signal decreased, and in the immunocompromised mice, it decreased at a slower rate than those with immunocompetent systems. Results were consistent with the performed immunohistochemistry. Here, imaging with ^{19}F-MRI provided an advantage over traditional postmortem tissue analysis by providing longitudinal cell information from the same animal. Another point of impact of this work is the fact that this is the first detailed report of the problem of the use of isoflurane as an anesthetic for preclinical cell tracking using PFCs.

Isoflurane and ^{19}F Cell Tracking

Isoflurane is a fluorinated anesthetic commonly used in experiments involving animal models and has the potential to corrupt signals originating from PFC-labeled cells due to buildup within fat/adipose tissue and potentially from within the lung. Isoflurane has two resonances that are very close to the resonances of PFCs commonly used in cell tracking (PFPE and PFCE) with values of −6.8 and −13.9 ppm relative to TFA (eg, PFPE is at −16 ppm relative to TFA).[85] A table of isoflurane chemical shifts relative to TFA in common solvents can be found here.[86] Relaxation times of these peaks depend on field strength and their local environments. T_2 is <5 ms in brain tissue[87] and longer in adipose tissue/fat where isoflurane can be deposited.[87,88]

The problem of isoflurane detection in animal models of PFC cell tracking is not widely discussed in the literature and where it is, mere avoidance of the ^{19}F signals from isoflurane is mentioned by using alternate anesthetics. Furthermore, image acquisition parameters helpful for pulse-sequence design to avoid exciting isoflurane are seldom given (eg, RF pulse shape and duration). Boehm-Sturm et al described the use of ketamine/xylazine maintained by syringe pump for their animal experiments to avoid the ^{19}F signals due to isoflurane.[33] van Heeswijk et al also acknowledged isoflurane as a potential problem and presented spectra showing peaks due to isoflurane in close proximity to PFCs, albeit at a signal strength an order of magnitude lower than those of the PFCs.[89] Ribot et al recently utilized pentobarbital rather than isoflurane to avoid isoflurane signal.[37] The first reported use of isoflurane in experiments involving cell-tracking applications was in 2010 in rats[76] and mice.[34] Before that, ketamine/xylazine was the preferred method of anesthesia presumably to avoid detection of isoflurane. Today, isoflurane is used extensively, even in cell-tracking applications, likely attributed to its ease of use in implementation.[25,27,30,39,40,46] With these reports and physical attributes in mind, it would seem that isoflurane is still very difficult to detect and may not be worth worrying about. However, working toward clinical translation, animal models will have to move to lower field strengths (≤3 T, reducing spectral separation in Hertz). This may require increases in scan time resulting in an increase in isoflurane deposition in fat due to reduced PFC SNR. More efficient imaging techniques will also increase sensitivity to low-density ^{19}F sources due to efficient use of SNR/t and shorter TE (eg, TE 1.8 ms[61]), which is simultaneously beneficial for detecting signals from both cells and isoflurane. Under these conditions, attention to isoflurane may be required using solutions such as shaped RF pulses employed to exclude excitation of unwanted peaks[61] or reversion to nonfluorinated anesthetics for animals. Figure 3 demonstrates the improvement (reduction of isoflurane signal) in ^{19}F images when considering excitation pulse parameters such as shape and pulse duration.

Clinical Cell Tracking

The first use of PFC-labeled cell tracking in human beings was recently demonstrated by Ahrens et al, who described the results of a phase I clinical trial in the United States using a DC vaccine designed for stage 4 colorectal cancer treatment.[57] Since the strength of treatment is proportional to the number of migrating DC, it is essential that researchers have a noninvasive, quantitative technique to monitor therapy. In addition, since lymph node removal is not practical in the clinical setting, imaging provides the only available information for dose optimization. Five patients were enrolled and assigned into groups of low dose ($N = 2$ at 1×10^6 cells) and high dose ($N = 3$ at 1×10^7 cells) labeled DC vaccines using clinical-grade PFC agent CS-1000. DCs were imaged using a FLASH sequence coregistered with ^{1}H images at 4 and 24 hours post transplant. Images obtained from this study are shown in Figure 4. Only the high-dose
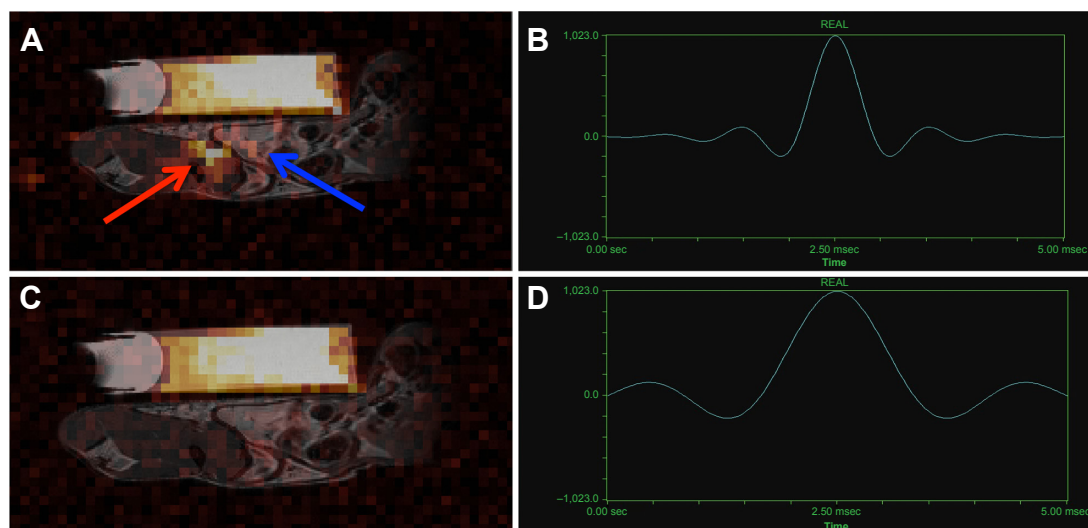
Figure 3. (**A**) Strong isoflurane signal (red arrow) is detectable following accumulation in the fat pads of mice after excitation with the standard Gaussian filtered sinc pulse (**B**). This signal is chemically shifted from the fat pad (blue arrow), compared to that of the reference tube above. (**C**) The mouse was then scanned with a non-filtered sinc pulse (**D**). Fourier transform of this pulse produces a narrower excitation that did not excite isoflurane ^{19}F atoms, reducing unwanted background signal from isoflurane. Both images have been windowed to the same level, and brightened to show the noise distribution. (**B**) The filtered pulse shape in time space is shown, with a width of 0.66 ms. (**D**) The non-filtered sinc pulse width is much broader with a FWHM of 1.32 ms in time space. Image courtesy of Gaudet et al[61] and reproduced with permission.

groups revealed detectable and countable cells. The cell counts at 4 hours were equivalent to the delivered dose and approximately half of that at 24 hours consistent with cell efflux from the initial injection site as cells migrate elsewhere. However, the signal was only detected at the injection site and not at the intended target organ: the draining lymph nodes. The significance of this work is that PFC-labeled cells using Food and Drug Administration-approved agents have been safely applied to human beings and were detected using MRI at 3 T as an important proof-of-principle experiment utilizing a DC vaccine.

### Lung Imaging Using Inert Fluorinated Gas MRI
^{19}F-based MRI has a role not just in imaging microbiological environments (cell tracking) but also within macrobiological environments, such as the lungs' airspaces. Lung MRI using inert fluorinated gases as contrast agents is another field enjoying recent success due to technological advancements for ^{19}F detection. Hyperpolarized (HP) noble gas MRI of the lung is a field that is >20 years old, born out of the desire to study the effect of anesthesia on brain function. The first HP gas lung image was obtained using MRI and HP ^{129}Xe in excised mouse lungs.[90] Since then, this field has flourished initially due to the success and ease of use of HP ^{3}He lung imaging. Together, these nuclei have been used to investigate and address various chronic respiratory diseases and acute lung injuries in both clinical studies and animal models, forming the basis of HP noble gas lung imaging. These gases have the ability to provide anatomical and functional information from within the lungs of human beings and rodents such as static ventilation imaging,[91] characterization of apparent diffusion coefficients

(ADCs),[92–96] and gas exchange, including those from models of emphysema, asthma, fibrosis, radiation-induced lung injury, and inflammation due to fungal spores.

HP gas MRI of the lung requires the use of expensive polarizers to achieve high SNR within the lung. In hyperpolarizing these isotopes, they receive enhancement of their nuclear polarization by a factor of 1×10^5 compared to their thermal equilibrium values resulting in their high SNR and excellent image quality. Furthermore, the isotopes used are also expensive and, in some cases, are becoming increasingly scarce (eg, ^{3}He). ^{3}He has been used quite extensively over the years; however, within the past decade, interest has shifted toward ^{129}Xe due to improved polarization techniques for ^{129}Xe,[97–99] ease in obtaining these isotopes, and ability to perform novel functional measurements such as gas exchange at the blood gas barrier,[100–102] perfusion measurements,[103] and brain function[104] due to ^{129}Xe's high solubility in tissues and blood compared with ^{3}He. ^{129}Xe has a natural abundance of 26% and small gyromagnetic ratio (~28% of ^{1}H). Though xenon is a valuable by-product of the liquid air industry and is quite easy to obtain, mixtures enriching the ^{129}Xe isotope can greatly increase SNR but at a much higher monetary cost.

Fluorinated gases require no such polarizer, are less costly to purchase, and the signal is derived from its thermal equilibrium polarization, just like conventional ^{1}H MRI. In addition, these gases comprise molecules possessing multiple NMR equivalent fluorine atoms collectively enhancing their detectability. The most common fluorinated gases used to date for lung imaging (especially in human beings) are SF_6 and C_3F_8. C_2F_6 has also been studied extensively in animal models
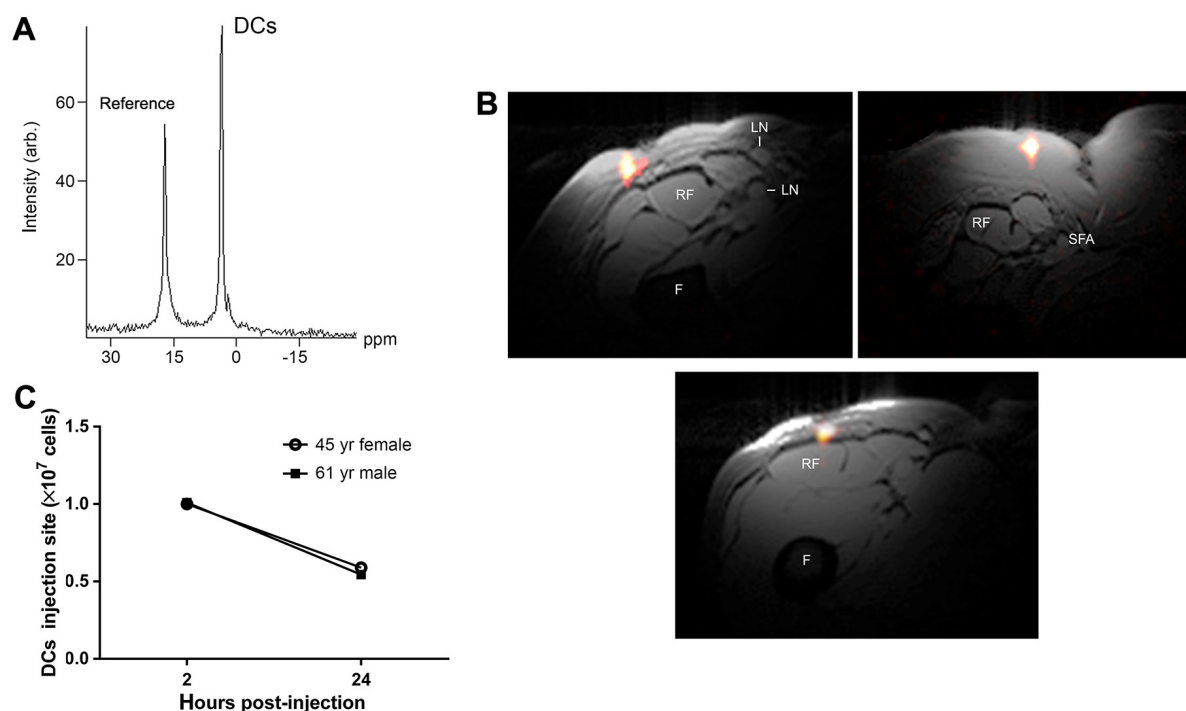
Figure 4. Result of the processes described in Figure 2 as applied to human cell tracking. In vivo MRI in patients following intradermal DC administration into quadriceps. In these patients, ~1 × 10⁷ labeled cells were injected. (**A**) A representative ^{19}F Magnetic Resonance Spectroscopy (MRS) spectrum of the patient at four hours postinoculation. The DCs appear as a single narrow peak. "Reference" is from an external tube containing TFA placed alongside the patient. (**B**) Axial composite ^{19}F/^{1}H images of the right thigh at 4 hours postinoculation in three patients, a 53-year-old female (left), a 45-year-old female (middle), and a 61-year-old male (right), where DCs are rendered in *hot-iron* pseudo color and the ^{1}H anatomy is displayed in rescale (F, femur; RF, rectus femoris; SFA, superficial femoral artery; LN, inguinal lymph node). (**C**) The results of the in vivo quantification of apparent cell numbers using the ^{19}F MRI data, measured in two patients. By 24 hours postinoculation, roughly half of the injected DCs were still present at the injection site. Image courtesy of Ahrens et al[57] and reproduced with permission.

and use of tetrafluoromethane (CF_4) has also been reported. These are not rare gases unlike ^{3}He and ^{129}Xe. Furthermore, use of these gases for MRI enables safe and repeatable imaging that is noninvasive, nonionizing and there is no ^{19}F background.

The first ^{19}F gas lung images were obtained in 1982 by Heidelberger and Lauterbur using CF_4 in excised rabbit lungs,[105] preceding the first HP gas lung images by 12 years. Shortly after, images were obtained in excised healthy canine lungs.[106,107] After a long gap in ^{19}F MRI lung reports, Kuethe et al demonstrated continuous breathing of C_2F_6 in rats,[108] and it was not until 10 years later that the first human lung images were reported by Wolf et al[6] using a mixture of SF_6 and oxygen. Though these gases currently produce images that are lower in quality compared with HP gas images, they come with many benefits, as described below. These gases are important because they provide similar diagnostic information and biomarkers as HP gases (eg, static ventilation images,[6,108–111] ADC,[112–117] and surface-to-volume ratio[114]) and complement them as alternative methods to probe healthy and diseased lungs.

Inert fluorinated gases are not the only methods available to perform MRI of the lung without the use of HP gases. For completeness, oxygen-enhanced methods,[118] Fourier decomposition,[119] and ^{1}H UTE[120] exist. Recent comprehensive reviews of lung imaging using MRI have been presented.[121–123]

Physical Properties, Hardware, Pulse Sequences, and Reconstruction

Of the commonly used fluorinated gases (ie, SF_6 and C_3F_8), there are several key physical properties that impact their effectiveness in the MRI of the lung. These include their relaxation times, spectral features, number of equivalent ^{19}F atoms, and diffusion properties. Table 1 summarizes the key properties for these gases and C_2F_6.

In general, the longitudinal relaxation times for these gases are short (1–30 ms). Bulk transverse relaxation times are even shorter with values less than a few milliseconds. SF_6 and C_3F_8 are recently reported gases used for human lung MRI. Just like their cell-tracking counterparts (PFCE and PFPE), SF_6 and C_3F_8 possess one resonance and two resonances, respectively. SF_6's single peak arises from six equivalent ^{19}F atoms with reported T_1 values of 1.2–2 ms[114,124] at 3 T and T_2^* values of 1s and 2.7 ms[124] in rat lungs[116] (3 and 4.7 T, respectively). On the other hand, C_3F_8 is more forgiving with slightly longer T_2^* values at the cost of handling a multispectral profile. A T_1 value of 12.4 ms (in human lungs)[109] and T_2^* values of 2.2 ms (in human lungs)[109] and 10 ms (in a resolution phantom)[124] have been reported at 3 T. Though C_3F_8 possesses two resonances separated by 48 ppm, to our knowledge, there does not seem to be any reported characterization of the

relaxation times of these peaks separately and the relaxation values reported are taken to be that of the main peak.

Unlike PFCs used for cell tracking, the diffusion coefficient of these ^{19}F gases plays an important role for probing lung microstructure and performing functional lung imaging. The theory and use of ^{19}F gases for diffusion-weighted MRI is extensively described in these reports.[112,113,115–117]

Fluorinated gases have a good record of safety due to their inertness, supported by their use in recent human imaging studies as inhaled contrast agents and lack of reported adverse events in the literature. Furthermore, these gases can be directly mixed with physiological concentrations of oxygen (21%) without large penalties in SNR, unlike HP gas agents.[113] The ability to create normoxic mixtures eliminates the risks involved with long-duration breath-holds of anoxic gas volumes and enables repeated breathing and even washout maneuvers in order to reach a steady state of ^{19}F gas within the lung as well as perform dynamic lung imaging.

The hardware challenges for ^{19}F lung imaging are similar to those for ^{19}F cell tracking. Amplifiers capable of excitation for a range of ^{19}F resonances (~150 ppm for ^{19}F gases[114]) are required as are dedicated RF coils capable of detecting the ^{19}F resonance. Lung imaging is commonly performed at clinical field strengths between 1.5 and 3 T. Imaging may prove difficult at higher field strengths due to the high magnetic susceptibility of lung tissue at the air–tissue interfaces. In fact, the theoretically predicted optimum field strength for HP gas human lung MRI is between 0.1 and 0.6 T.[125] Specific absorption rate (SAR) depends on the field strength and may impose additional safety restrictions at field strengths >3 T. RF coils capable of detecting both ^{1}H and ^{19}F signals are desirable for both preclinical and clinical imaging, though designs exist that allow the use of the scanners' native body coil for ^{1}H by actively detuning the ^{19}F coil without removal of the coil or patient.[109,110,126] Furthermore, the spatial extent of ^{19}F signals is quite larger in comparison with cell-tracking applications (eg, 5 L lung volume vs. 1 mL injection sites) requiring different RF coil solutions such as large volume coils of birdcage design or flexible surface coils. Unlike cell tracking, which for some applications requires minimal penetration depth (~1–2 cm), lung imaging requires uniform excitation of the entire lung, requiring high transmit uniformity and power. Birdcage designs have been employed for [3]He,[91,127] [129]Xe,[128] and [23]Na,[129] but to our knowledge, no ^{19}F coils of this design have been reported. The use of a coil of this type for ^{19}F lung imaging would provide high B_1 uniformity and require less effort in setup from patient to patient. Other reported coils used for ^{19}F lung imaging employ flexible volume coils with a detuning circuit to allow for ^{1}H body coil imaging.[109,130] This design allows for easy imaging between ^{1}H and ^{19}F frequencies and also provides patient comfort. Due to the flexibility of the coil, however, B_1 mapping is required on a case basis in order to correct the images for inhomogeneous B_1 between patients.

Due to the short relaxation times of these gases, MR pulse sequences having short repetition time (TR) and TE are desirable. The shorter TR reduces the overall scan time providing a time-saving that can then be used to enhance SNR by rapid signal averaging (subject to specific absorption rate limitations). Several sequences used for imaging ^{19}F gases have been described in the literature, including 3D gradient recalled echo (GRE),[110,130,131] 2D/3D FLASH,[6,132] UTE,[109] COMSPIRA,[94,116,117] and X-centric, a type of GRE.[124] UTE and 3D GRE methods have been compared demonstrating improvements in SNR for UTE at the cost of edge resolution.[131] X-centric has also been compared to UTE and GRE methods in a resolution phantom demonstrating both improvements in SNR and sustained resolution compared with UTE and GRE at the cost of a second scan (because only 50.5% of k-space is collected per readout gradient polarity). COMSPIRA is a hybrid sequence merging projection reconstruction and spiral readouts. It is insensitive to motion due to the use of oversampling of the low spatial frequencies in k-space and has been used to measure ADC maps in rats.

Isoflurane and [19]F Lung Imaging

Though isoflurane is in common use as an anesthetic for animal models used in cell tracking, there is no description of isoflurane posing a problem for ^{19}F lung imaging. This is likely due to the fact that the described preclinical research in rats and pigs all used injectable anesthetics such as sodium pentobarbital, ketamine, xylazine, and thiopental rather than inhaled anesthetics such as isoflurane and halothane to deliberately avoid ^{19}F signals from their anesthetics.

Static Lung Imaging

Static ventilation lung imaging is the easiest and most common method of lung imaging to perform. In general, a volume of inert fluorinated gas is introduced to the lungs using a ventilator (for animals) or inhaled from a plastic bag (for human beings) as depicted in Figure 5. In either case, once the dose is delivered, the animal/human being engages in a breath-hold and MRI is performed during a modest breath-hold length of up to 15 seconds. During the breath-hold, motion artifacts or blurring due to breathing are of no concern due to the temporarily suspended respiratory motion. The gas is then exhaled and the experiment can be repeated. In some cases, the volume of the lung is washed out using prebreaths of ^{19}F gas before the imaging breath-hold is initiated in order to provide a uniform distribution of inert fluorinated gas to all possible air spaces. There may be inherent differences in lung volume between ^{19}F images and ^{1}H due to the fact that separate breath-holds are needed for each. These differences are controlled to the best of the researcher's ability (eg, functional residual capacity (FRC) + 1 L of ^{19}F gas or air). The first ^{19}F gas lung images obtained by Heidelberger and Lauterbur in 1982[105] as well as those demonstrated by Rinck[106,107] and Keuthe,[108] are the first examples of static lung imaging.
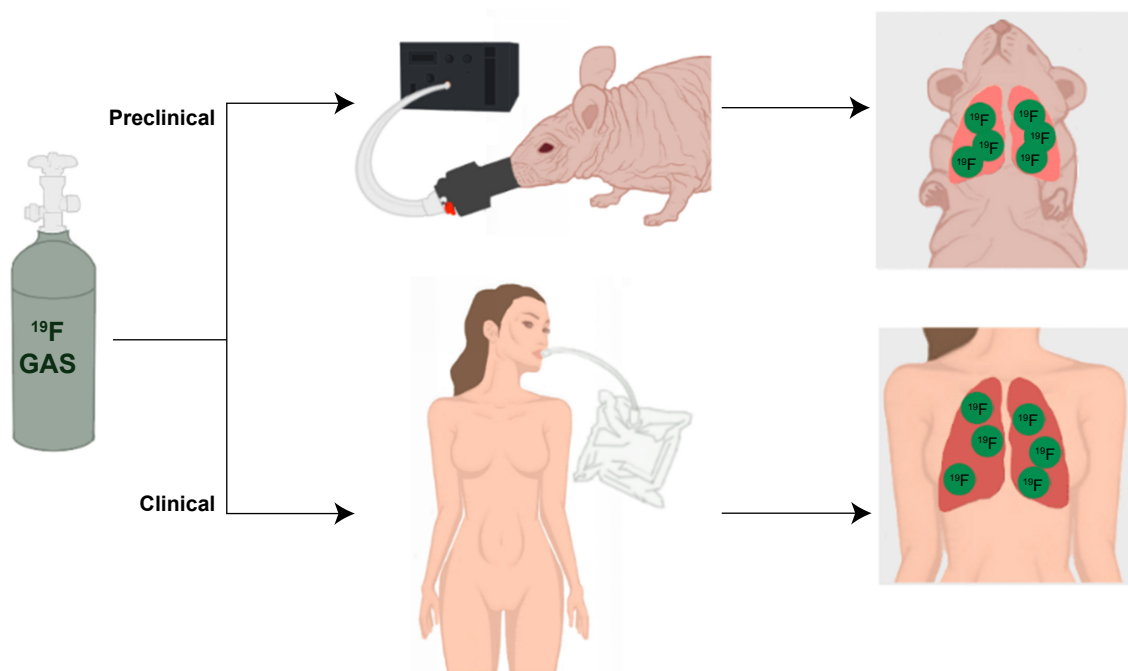
Figure 5. Medical-grade inert fluorinated gases are provided by compressed gas companies and are ready to use straight from the cylinders unlike HP ^{3}He and ^{129}Xe. Animals and human beings are administered these gases either using a specialized animal ventilator or from bags containing large volumes of gas (1–5 L), which patients inhale from. During a breath-hold, imaging of the inert fluorinated gases is performed, which reveals information of the ventilated airspaces of the lungs.

Dynamic Lung Imaging

Dynamic lung imaging using fluorinated gases was first described by Schreiber et al using SF_6 in pig lungs to measure wash-in and washout kinetics using dynamic gradient echo imaging.[133] Kuethe et al measured the volume of rat lungs during the respiratory cycle of mechanically ventilated rats using SF_6 in a disease model of elastase-induced emphysema.[134] By calibrating NMR signal strength to known volumes of SF_6 within the laboratory, fast spectroscopic techniques can be used to measure in vivo lung volume with high temporal resolution (20 measurements per second). Wolf et al investigated MRI of dynamic wash-in of fluorinated gas using C_2F_6 in pig lungs to optimize image acquisition for very short acquisition times with respectable image quality in as short as two seconds.[132] They also investigated C_3F_8 in a lung washout study and, for the first time, demonstrated and quantified washout dynamics under high-frequency oscillatory ventilation. Scholz et al compared ^{19}F gas-derived measurements of lung function and did a direct comparison with nonimaging respiratory gas analysis measuring alveolar gas fraction in pigs. Ouriadov et al investigated and compared ventilation mapping using SF_6 and PFP after establishing improved resolution and SNR using the X-centric pulse sequence compared with UTE and fast gradient recalled echo (FGRE) within a resolution phantom. X-centric can achieve relatively short TE (~0.5 ms) while maintaining the benefits of Cartesian style acquisition.[124]

Functional Lung Imaging (Diffusion, paO2, Fractional Ventilation, and Gradients)

Expanding on the possible detectable biomarkers using fluorinated gases for lung MRI, ADCs of gases,[114–117,135] oxygen partial pressure (paO2), ventilation perfusion (V/Q) measurements,[111,136] and fractional ventilation parameter (r) and r gradients[124] have been reported. The first application of diffusion weighted imaging using ^{19}F in excised human lungs was reported by Jacob et al.[115] C_2F_6 was used to distinguish between healthy and emphysematous excised human lungs and described the benefits of C_2F_6 over SF_6, CF_4, and C_3F_8 for ADC measurements due to its favorable relaxation times, monochromatic spectrum, and diffusion coefficient. Pérez-Sánchez et al demonstrated the first in vivo ADC maps in an animal model using rats breathing SF_6 at 4.7 T.[116] They reported adequate SNR for the formation of ADC maps as well as a protocol to keep imaging time short. Kuethe et al demonstrated the use and sensitivity of SF_6 in a rat model of obstructed lungs to measure oxygen partial pressure.[111] Regions of poor V/Q ratio appeared brighter within images due to their shortened T_1 due to the higher concentrations of oxygen (poor gas exchange). Ouriadov et al were the first to use and compare SF_6 and C_3F_8 to generate r maps[137,138] and calculate the gravitational dependence of r in rat lungs.[124] They demonstrated that the use of either gas was suitable for these functional measurements within rats with sufficient SNR and may be translatable to clinical scale imaging.
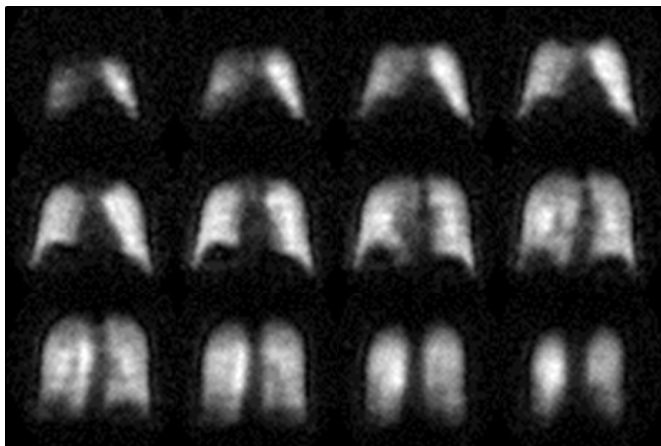
Figure 6. Coronal pulmonary ^{19}F 3D UTE MR images obtained from a healthy volunteer during a 15 second breath-hold after continuous breathing from a 5 L mixture of 79% PFP and 21% oxygen followed by a 1 L inhalation of the same mixture in order to image lungs at FRC + 1 L with an equilibrium distribution of the inert gas mixture. Image courtesy of Couch et al[109] and reproduced with permission.

Clinical Lung Imaging

The first human lung images obtained using ^{19}F gas were reported by Wolf et al[6] using a mixture of SF_6 and oxygen. Recent static ventilation imaging in human beings has been reported using enhanced techniques to overcome the low sensitivity of ^{19}F gas lung imaging. The use of a large pre-washout of the lungs by inhaling several breaths of fluorinated gas mixed with 21% oxygen from bags[130] or delivery system (Physiorack)[126] greatly increases the number of ^{19}F spins within the lungs prior to imaging. Couch et al utilized a large 5 L bag of gas (C_3F_8 or SF_6 mixed with 21% of oxygen) to washout lungs prior to inhalation of 1 L of gas from a second bag to ensure imaging was carried out at FRC + 1 L.[109] They employed an UTE imaging sequence (3D UTE) and compared the results with the previously reported FGRE images reporting a factor of 2 enhancement in SNR. Representative UTE images are shown in Figure 6.

Halaweish et al performed the first ^{19}F enhanced dynamic imaging studies on healthy volunteers and volunteers with emphysema and chronic obstructive pulmonary disease, demonstrating differences in ventilation heterogeneity and gas trapping in those with chronic obstructive pulmonary disease.[110] Due to the short relaxation times of these fluorinated gases, sequences employing shorter TEs can greatly impact SNR in a beneficial way. Finally, measurement of surface-to-volume ratios[114] and gravitational gradients[114] have also been demonstrated in human lungs using PFP; however, a full study comparing healthy lungs with diseased lungs remains to be reported.

Conclusions

The use of fluorinated contrast agents for MRI of cell tracking, lung imaging, and drug development represents a large body of scientific research. Various problems and solutions,

owing to the range of field strengths (1.5–11.7 T) that this research spans across, the relaxation properties of different fluorinated contrast agents, and practical issues have been described. UTE strategies, isoflurane usage, and detection of ^{19}F agents at clinical field strengths are where cell tracking and lung imaging may mutually benefit each other. Cell tracking may benefit from the development of UTE strategies for lung imaging, which may improve detection of ^{19}F-labeled cells in the presence of iron for multicell population labelling (eg, Hitchens et al[62]). Preclinical ^{19}F lung imaging does not utilize isoflurane at all. Alternate anesthesia strategies would eliminate the problems that isoflurane may cause for cell tracking. With clinical translation in mind, cell tracking may greatly benefit from technological advances in lung imaging since the majority of research in that field is performed at 1.5 and 3 T. Novel RF coils and arrays have been developed as well as pulse sequences designed to detect low concentrations of ^{19}F. Fluorinated contrast agents are indeed versatile contrast agents well suited for probing the micro- to macrobiological environments, and future work will only enhance their utility in these important fields.

Acknowledgment

Author Contributions

REFERENCES

1. Gorter CJ, Broer LJF. Negative result of an attempt to observe nuclear magnetic resonance in solids. *Physica*. 1942;9(6):591–596.
2. Holland GN, Bottomley A, Hinshaw WS. ^{19}F magnetic resonance imaging. *J Magn Reson*. 1977;28(1):133–136.
3. Tran HT, Guo Q, Schumacher DJ, Buxton RB, Mattrey RF. ^{19}F chemical shift imaging technique to measure intracellular pO2 in vivo using perflubron. *Acad Radiol*. 1995;2(9):756–761.
4. Ahrens ET, Flores R, Xu H, Morel PA. In vivo imaging platform for tracking immunotherapeutic cells. *Nat Biotechnol*. 2005;23(8):983–987.
5. Brix G, Bellemann ME, Haberkorn U, Gerlach L, Bachert P, Lorenz WJ. Mapping the biodistribution and catabolism of 5-fluorouracil in tumor-bearing rats by chemical-shift selective ^{19}F MR imaging. *Magn Reson Med*. 1995;34(3):302–307.
6. Wolf U, Scholz A, Terekhov M, et al. Fluorine-19 MRI of the lung: first human experiment. *International Society for Magnetic Resonance Imaging Proceedings*. Toronto, Ontario, Canada; 2008.
7. Bartusik D, Aebisher D. 19(F) applications in drug development and imaging—a review. *Biomed Pharmacother*. 2014;68(6):813–817.
8. Ntziachristos V. Fluorescence molecular imaging. *Annu Rev Biomed Eng*. 2006; 8:1–33.
9. Phelps ME. Molecular imaging with positron emission tomography. *Annu Rev Nucl Part Sci*. 2002;52(1):303–338.
10. Stodilka RZ, Blackwood KJ, Kong H, Prato FS. A method for quantitative cell tracking using SPECT for the evaluation of myocardial stem cell therapy. *Nucl Med Commun*. 2006;27(10):807–813.
11. Stodilka RZ, Blackwood KJ, Prato FS. Tracking transplanted cells using dual-radionuclide SPECT. *Phys Med Biol*. 2006;51(10):2619–2632.

12. Bulte JW, Hoekstra Y, Kamman RL, et al. Specific MR imaging of human lymphocytes by monoclonal antibody-guided dextran-magnetite particles. *Magn Reson Med*. 1992;25(1):148–157.

13. Bulte JW, Ma LD, Magin RL, et al. Selective MR imaging of labeled human peripheral blood mononuclear cells by liposome mediated incorporation of dextran-magnetite particles. *Magn Reson Med*. 1993;29(1):32–37.

14. Yeh TC, Zhang W, Ildstad ST, Ho C. Intracellular labeling of T-cells with superparamagnetic contrast agents. *Magn Reson Med*. 1993;30(5):617–625.

15. Strobel K, Hoerr V, Schmid F, Wachsmuth L, Löffler B, Faber C. Early detection of lung inflammation: exploiting T1-effects of iron oxide particles using UTE MRI. *Magn Reson Med*. 2012;68(6):1924–1931.

16. Zhou R, Idiyatullin D, Moeller S, et al. SWIFT detection of SPIO-labeled stem cells grafted in the myocardium. *Magn Reson Med*. 2010;63(5):1154–1161.

17. Heyn C, Ronald JA, Mackenzie LT, et al. In vivo magnetic resonance imaging of single cells in mouse brain with optical validation. *Magn Reson Med*. 2006; 55(1):23–29.

18. Shapiro EM, Medford-Davis LN, Fahmy TM, Dunbar CE, Koretsky AP. Antibody-mediated cell labeling of peripheral T cells with micron-sized iron oxide particles (MPIOs) allows single cell detection by MRI. *Contrast Media Mol Imaging*. 2007;2(3):147–153.

19. Ribot EJ, Foster PJ. In vivo MRI discrimination between live and lysed iron-labelled cells using balanced steady state free precession. *Eur Radiol*. 2012;22(9): 2027–2034.

20. Ahrens ET, Bulte JW. Tracking immune cells in vivo using magnetic resonance imaging. *Nat Rev Immunol*. 2013;13(10):755–763.

21. Dekaban GA, Hamilton AM, Fink CA, et al. Tracking and evaluation of dendritic cell migration by cellular magnetic resonance imaging. *Wiley Interdiscip Rev Nanomed Nanobiotechnol*. 2013;5(5):469–483.

22. Srinivas M, Heerschap A, Ahrens ET, Figdor CG, de Vries IJ. (19)F MRI for quantitative in vivo cell tracking. *Trends Biotechnol*. 2010;28(7):363–370.

23. Yu JX, Hallac RR, Chiguru S, Mason RP. New frontiers and developing applications in ¹⁹F NMR. *Prog Nucl Magn Reson Spectrosc*. 2013;70:25–49.

24. Bulte JW. Hot spot MRI emerges from the background. *Nat Biotechnol*. 2005; 23(8):945–946.

25. Waiczies H, Lepore S, Janitzek N, et al. Perfluorocarbon particle size influences magnetic resonance signal and immunological properties of dendritic cells. *PLoS One*. 2011;6(7):e21981.

26. Ahrens ET, Young WB, Xu H, Pusateri LK. Rapid quantification of inflammation in tissue samples using perfluorocarbon emulsion and fluorine-19 nuclear magnetic resonance. *Biotechniques*. 2011;50(4):229–234.

27. Balducci A, Helfer BM, Ahrens ET, O'Hanlon CF 3rd, Wesa AK. Visualizing arthritic inflammation and therapeutic response by fluorine-19 magnetic resonance imaging (¹⁹F MRI). *J Inflamm (Lond)*. 2012;9(1):24.

28. Ebner B, Behm P, Jacoby C, et al. Early assessment of pulmonary inflammation by ¹⁹F MRI in vivo. *Circ Cardiovasc Imaging*. 2010;3(2):202–210.

29. Flögel U, Ding Z, Hardung H, et al. In vivo monitoring of inflammation after cardiac and cerebral ischemia by fluorine magnetic resonance imaging. *Circulation*. 2008;118(2):140–148.

30. Hertlein T, Sturm V, Kircher S, et al. Visualization of abscess formation in a murine thigh infection model of *Staphylococcus aureus* by ¹⁹F-magnetic resonance imaging (MRI). *PLoS One*. 2011;6(3):e18246.

31. Jacoby C, Temme S, Mayenfels F, et al. Probing different perfluorocarbons for in vivo inflammation imaging by ¹⁹F MRI: image reconstruction, biological half-lives and sensitivity. *NMR Biomed*. 2014;27(3):261–271.

32. Bible E, Dell'Acqua F, Solanky B, et al. Non-invasive imaging of transplanted human neural stem cells and ECM scaffold remodeling in the stroke-damaged rat brain by ¹⁹F—and diffusion-MRI. *Biomaterials*. 2012;33(10):2858–2871.

33. Boehm-Sturm P, Mengler L, Wecker S, Hoehn M, Kallur T. In vivo tracking of human neural stem cells with ¹⁹F magnetic resonance imaging. *PLoS One*. 2011;6(12):e29040.

34. Helfer BM, Balducci A, Nelson AD, et al. Functional assessment of human dendritic cells labeled for in vivo (19)F magnetic resonance imaging cell tracking. *Cytotherapy*. 2010;12(2):238–250.

35. Helfer BM, Balducci A, Sadeghi Z, et al. (1)(9)F MRI tracer preserves in vitro and in vivo properties of hematopoietic stem cells. *Cell Transplant*. 2013;22(1): 87–97.

36. Muhammad G, Jablonska A, Rose L, Walczak P, Janowski M. Effect of MRI tags: SPIO nanoparticles and ¹⁹F nanoemulsion on various populations of mouse mesenchymal stem cells. *Acta Neurobiol Exp (Wars)*. 2015;75(2):144–159.

37. Ribot EJ, Gaudet JM, Chen Y, Gilbert KM, Foster PJ. In vivo MR detection of fluorine-labeled human MSC using the bSSFP sequence. *Int J Nanomedicine*. 2014;9:1731–1739.

38. Janjic JM, Srinivas M, Kadayakkara DK, Ahrens ET. Self-delivering nanoemulsions for dual fluorine-19 MRI and fluorescence detection. *J Am Chem Soc*. 2008;130(9):2832–2841.

39. Hertlein T, Sturm V, Jakob P, Ohlsen K. ¹⁹F magnetic resonance imaging of perfluorocarbons for the evaluation of response to antibiotic therapy in a *Staphylococcus aureus* infection model. *PLoS One*. 2013;8(5):e64440.

40. Kadayakkara DK, Ranganathan S, Young WB, Ahrens ET. Assaying macrophage activity in a murine model of inflammatory bowel disease using fluorine-19 MRI. *Lab Invest*. 2012;92(4):636–645.

41. Bonetto F, Srinivas M, Weigelin B, et al. A large-scale ¹⁹F MRI-based cell migration assay to optimize cell therapy. *NMR Biomed*. 2012;25(9):1095–1103.

42. Jacoby C, Borg N, Heusch P, et al. Visualization of immune cell infiltration in experimental viral myocarditis by (19)F MRI in vivo. *MAGMA*. 2014; 27(1):101–106.

43. Ruiz-Cabello J, Walczak P, Kedziorek DA, et al. In vivo "hot spot" MR imaging of neural stem cells using fluorinated nanoparticles. *Magn Reson Med*. 2008; 60(6):1506–1511.

44. Waiczies H, Lepore S, Drechsler S, et al. Visualizing brain inflammation with a shingled-leg radio-frequency head probe for ¹⁹F/¹H MRI. *Sci Rep*. 2013;3:1280.

45. Balducci A, Wen Y, Zhang Y, et al. A novel probe for the non-invasive detection of tumor-associated inflammation. *Oncoimmunology*. 2013;2(2):e23034.

46. Hitchens TK, Ye Q, Eytan DF, Janjic JM, Ahrens ET, Ho C. ¹⁹F MRI detection of acute allograft rejection with in vivo perfluorocarbon labeling of immune cells. *Magn Reson Med*. 2011;65(4):1144–1153.

47. Weise G, Basse-Luesebrink TC, Wessig C, Jakob PM, Stoll G. In vivo imaging of inflammation in the peripheral nervous system by (19)F MRI. *Exp Neurol*. 2011;229(2):494–501.

48. Tirotta I, Mastropietro A, Cordiglieri C, et al. A superfluorinated molecular probe for highly sensitive in vivo(19)F -MRI. *J Am Chem Soc*. 2014;136(24):8524–8527.

49. Jiang ZX, Liu X, Jeong EK, Yu YB. Symmetry-guided design and fluorous synthesis of a stable and rapidly excreted imaging tracer for (19)F MRI. *Angew Chem Int Ed Engl*. 2009;48(26):4755–4758.

50. Mastropietro A, Cordiglieri C, Tirotta I, et al. ¹⁹F-MRI applications of PERFECTA at 7T: characterization studies on phantoms and on in vitro fibroblasts and T cells. *International Society for Magnetic Resonance Imaging Proceedings*. Toronto, Ontario, Canada; 2015.

51. Srinivas M, Boehm-Sturm P, Figdor CG, de Vries IJ, Hoehn M. Labeling cells for in vivo tracking using (19)F MRI. *Biomaterials*. 2012;33(34):8830–8840.

52. Krafft MP. Fluorocarbons and fluorinated amphiphiles in drug delivery and biomedical research. *Adv Drug Deliv Rev*. 2001;47(2–3):209–228.

53. Srinivas M, Morel PA, Ernst LA, Laidlaw DH, Ahrens ET. Fluorine-19 MRI for visualization and quantification of cell migration in a diabetes model. *Magn Reson Med*. 2007;58(4):725–734.

54. Gaudet JM, Fox FC, Wade MS, et al. *Development of Clinical 19F-MRI Cell Tracking for Cancer Immunotherapy*. Toronto: Ontario Institute for Cancer Research Scientific Meeting; 2015.

55. Kok MB, de Vries A, Abdurrachim D, et al. Quantitative (1)H MRI, (19)F MRI, and (19)F MRS of cell-internalized perfluorocarbon paramagnetic nanoparticles. *Contrast Media Mol Imaging*. 2011;6(1):19–27.

56. Kadayakkara DK, Damodaran K, Hitchens TK, Bulte JW, Ahrens ET. (19)F spin-lattice relaxation of perfluoropolyethers: dependence on temperature and magnetic field strength (7.0–14.1T). *J Magn Reson*. 2014;242:18–22.

57. Ahrens ET, Helfer BM, O'Hanlon CF, Schirda C. Clinical cell therapy imaging using a perfluorocarbon tracer and fluorine-19 MRI. *Magn Reson Med*. 2014; 72(6):1696–1701.

58. Partlow KC, Chen J, Brant JA, et al. ¹⁹F magnetic resonance imaging for stem/progenitor cell tracking with multiple unique perfluorocarbon nanobeacons. *FASEB J*. 2007;21(8):1647–1654.

59. Weibel S, Basse-Luesebrink TC, Hess M, et al. Imaging of intratumoral inflammation during oncolytic virotherapy of tumors by 19F-magnetic resonance imaging (MRI). *PLoS One*. 2013;8(2):e56317.

60. van Heeswijk RB, De Blois J, Kania G, et al. Selective in vivo visualization of immune-cell infiltration in a mouse model of autoimmune myocarditis by fluorine-19 cardiac magnetic resonance. *Circ Cardiovasc Imaging*. 2013;6(2): 277–284.

61. Gaudet JM, Ribot EJ, Chen Y, Gilbert KM, Foster PJ. Tracking the fate of stem cell implants with fluorine-19 MRI. *PLoS One*. 2015;10(3):e0118544.

62. Hitchens TK, Liu L, Foley LM, Simplaceanu V, Ahrens ET, Ho C. Combining perfluorocarbon and superparamagnetic iron-oxide cell labeling for improved and expanded applications of cellular MRI. *Magn Reson Med*. 2015;73(1):367–375.

63. Giraudeau C, Flament J, Marty B, et al. A new paradigm for high-sensitivity 19F magnetic resonance imaging of perfluorooctylbromide. *Magn Reson Med*. 2010;63(4):1119–1124.

64. Gudbjartsson H, Patz S. The Rician distribution of noisy MRI data. *Magn Reson Med*. 2005;34(6):910–914.

65. Meissner M, Reisert M, Hugger T, Hennig J, von Elverfeldt D, Leupold J. Revealing signal from noisy (19) F MR images by chemical shift artifact correction. *Magn Reson Med*. 2015;73(6):2225–2233.

66. Lustig M, Donoho D, Pauly JM. Sparse MRI: the application of compressed sensing for rapid MR imaging. *Magn Reson Med*. 2007;58(6):1182–1195.

67. Kampf T, Fischer A, Basse-Lüsebrink TC, et al. Application of compressed sensing to in vivo 3D ¹⁹F CSI. *J Magn Reson*. 2010;207(2):262–273.

68. Zhong J, Mills PH, Hitchens TK, Ahrens ET. Accelerated fluorine-19 MRI cell tracking using compressed sensing. *Magn Reson Med*. 2013;69(6):1683–1690.

69. Keupp J, Rahmer J, Grässlin I, et al. Simultaneous dual-nuclei imaging for motion corrected detection and quantification of 19F imaging agents. *Magn Reson Med*. 2011;66(4):1116–1122.

70. Bönner F, Merx MW, Klingel K, et al. Monocyte imaging after myocardial infarction with ¹⁹F MRI at 3 T: a pilot study in explanted porcine hearts. *Eur Heart J Cardiovasc Imaging*. 2015;16(6):612–620.

71. Temme S, Jacoby C, Ding Z, et al. Technical advance: monitoring the trafficking of neutrophil granulocytes and monocytes during the course of tissue inflammation by noninvasive ¹⁹F MRI. *J Leukoc Biol*. 2014;95(4):689–697.

72. Weise G, Basse-Lüsebrink TC, Kleinschnitz C, Kampf T, Jakob PM, Stoll G. In vivo imaging of stepwise vessel occlusion in cerebral photothrombosis of mice by ¹⁹F MRI. *PLoS One*. 2011;6(12):e28143.

73. Vasudeva K, et al. Imaging neuroinflammation in vivo in a neuropathic pain rat model with near-infrared fluorescence and ¹⁹F magnetic resonance. *PLoS One*. 2014;9(2):e90589.

74. Hertlein T, Sturm V, Lorenz U, Sumathy K, Jakob P, Ohlsen K. Bioluminescence and ¹⁹F magnetic resonance imaging visualize the efficacy of lysostaphin alone and in combination with oxacillin against *Staphylococcus aureus* in murine thigh and catheter-associated infection models. *Antimicrob Agents Chemother*. 2014; 58(3):1630–1638.

75. Chen S, Yang Y, Li H, Zhou X, Liu M. pH-Triggered Au-fluorescent mesoporous silica nanoparticles for ¹⁹F MR/fluorescent multimodal cancer cellular imaging. *Chem Commun (Camb)*. 2014;50(3):283–285.

76. Kadayakkara DK, Janjic JM, Pusateri LK, Young WB, Ahrens ET. In vivo observation of intracellular oximetry in perfluorocarbon-labeled glioma cells and chemotherapeutic response in the CNS using fluorine-19 MRI. *Magn Reson Med*. 2010;64(5):1252–1259.

77. Patrick MJ, Janjic JM, Teng H, et al. Intracellular pH measurements using perfluorocarbon nanoemulsions. *J Am Chem Soc*. 2013;135(49):18445–18457.

78. Zhong J, Sakaki M, Okada H, Ahrens ET. In vivo intracellular oxygen dynamics in murine brain glioma and immunotherapeutic response of cytotoxic T cells observed by fluorine-19 magnetic resonance imaging. *PLoS One*. 2013;8(5):e59479.

79. Dewitte H, Geers B, Liang S, et al. Design and evaluation of theranostic perfluorocarbon particles for simultaneous antigen-loading and ¹⁹F-MRI tracking of dendritic cells. *J Control Release*. 2013;169(1):141–149.

80. Waiczies H, Guenther M, Skodowski J, et al. Monitoring dendritic cell migration using 19F/1H magnetic resonance imaging. *J Vis Exp*. 2013;(73):e50251–e50251.

81. Srinivas M, Turner MS, Janjic JM, Morel PA, Laidlaw DH, Ahrens ET. In vivo cytometry of antigen-specific t cells using ¹⁹F MRI. *Magn Reson Med*. 2009; 62(3):747–753.

82. Ludwig KD, Bouchlaka M, Gordon J, Capitini C, Fain SB. In vivo quantification of human natural killer cells by 19F MRI. *International Society for Magnetic Resonance Imaging Proceedings*. Toronto, Ontario, Canada; 2015.

83. Chagastelles PC, Nardi NB, Camassola M. Biology and applications of mesenchymal stem cells. *Sci Prog*. 2010;93(pt 2):113–127.

84. Pittenger MF, Mackay AM, Beck SC, et al. Multilineage potential of adult human mesenchymal stem cells. *Science*. 1999;284(5411):143–147.

85. McFarland E, Koutcher JA, Rosen BR, Teicher B, Brady TJ. In vivo 19F NMR imaging. *J Comput Assist Tomogr*. 1985;9(1):8–15.

86. Wyrwicz AM, Pszenny MH, Schofield JC, Tillman PC, Gordon RE, Martin PA. Noninvasive observations of fluorinated anesthetics in rabbit brain by fluorine-19 nuclear magnetic resonance. *Science*. 1983;222(4622):428–430.

87. Venkatasubramanian PN, Shen YJ, Wyrwicz AM. Characterization of the cerebral distribution of general anesthetics in vivo by two-dimensional ¹⁹F chemical shift imaging. *Magn Reson Med*. 1996;35(4):626–630.

88. Becker DE, Rosenberg M. Nitrous oxide and the inhalation anesthetics. *Anesth Prog*. 2008;55(4):124–130. quiz 131–2.

89. van Heeswijk RB, Pilloud Y, Flögel U, Schwitter J, Stuber M. Fluorine-19 magnetic resonance angiography of the mouse. *PLoS One*. 2012;7(7):e42236.

90. Albert MS, Cates GD, Driehuys B, Happer W, Saam B, Wishnia A. Biological magnetic resonance imaging using laser-polarized 129Xe. *Nature*. 1994; 370(6486):199–201.

91. Parraga G, Ouriadov A, Evans A, et al. Hyperpolarized 3He ventilation defects and apparent diffusion coefficients in chronic obstructive pulmonary disease: preliminary results at 3.0 Tesla. *Invest Radiol*. 2007;42(6):384–391.

92. Yablonskiy DA, Sukstanskii AL, Woods JC, et al. Quantification of lung microstructure with hyperpolarized 3He diffusion MRI. *J Appl Physiol (1985)*. 2009;107(4):1258–1265.

93. Sukstanskii AL, Yablonskiy DA. In vivo lung morphometry with hyperpolarized 3He diffusion MRI: theoretical background. *J Magn Reson*. 2008;190(2): 200–210.

94. Rodríguez I, Pérez-Sánchez JM, Peces-Barba G, Kaulisch T, Stiller D, Ruiz-Cabello J. Long-range diffusion of hyperpolarized 3He in rats. *Magn Reson Med*. 2009;61(1):54–58.

95. Woods JC, Yablonskiy DA, Choong CK, et al. Long-range diffusion of hyperpolarized 3He in explanted normal and emphysematous human lungs via magnetization tagging. *J Appl Physiol (1985)*. 2005;99(5):1992–1997.

96. Yablonskiy DA, Sukstanskii AL, Leawoods JC, et al. Quantitative in vivo assessment of lung microstructure at the alveolar level with hyperpolarized 3He diffusion MRI. *Proc Natl Acad Sci U S A*. 2002;99(5):3111–3116.

97. Driehuys B. High-volume production of laser polarized 129Xe. *Appl Phys Lett*. 1996;69(12):3.

98. Hersman FW, Ruset IC, Ketel S, et al. Large production system for hyperpolarized 129Xe for human lung imaging studies. *Acad Radiol*. 2008;15(6):683–692.

99. Nikolaou P, Coffey AM, Walkup LL, et al. XeNA: an automated 'open-source' (129)Xe hyperpolarizer for clinical use. *Magn Reson Imaging*. 2014;32(5):541–550.

100. Driehuys B, Cofer GP, Pollaro J, Mackel JB, Hedlund LW, Johnson GA. Imaging alveolar-capillary gas transfer using hyperpolarized 129Xe MRI. *Proc Natl Acad Sci U S A*. 2006;103(48):18278–18283.

101. Månsson S, Wolber J, Driehuys B, Wollmer P, Golman K. Characterization of diffusing capacity and perfusion of the rat lung in a lipopolysaccharide disease model using hyperpolarized 129Xe. *Magn Reson Med*. 2003;50(6):1170–1179.

102. Fox MS, Ouriadov A, Thind K, et al. Detection of radiation induced lung injury in rats using dynamic hyperpolarized (129)Xe magnetic resonance spectroscopy. *Med Phys*. 2014;41(7):072302.

103. Zhou X, Sun Y, Mazzanti M, et al. MRI of stroke using hyperpolarized 129Xe. *NMR Biomed*. 2011;24(2):170–175.

104. Mazzanti ML, Walvick RP, Zhou X, et al. Distribution of hyperpolarized xenon in the brain following sensory stimulation: preliminary MRI findings. *PLoS One*. 2011;6(7):e21607.

105. Heidelberger E, Lauterbur PC. Gas phase 19F-NMR zeugmatography: a new approach to lung ventilation imaging. *International Society for Magnetic Resonance Imaging Proceedings*. Publisher Wiley (ISMRM). Boston, Massacheusetts; 1982:70–71.

106. Rinck PA, Petersen SB, Heidelberger E, et al. NMR ventilation imaging of the lungs using perfluorinated gases. In *Magnetic Resonance in Medicine*. Williams & Wilkins. West Camden St, Baltimore, MD; 1984;1(2):237–237.

107. Rinck PA, Petersen SB, Lauterbur PC. [NMR imaging of fluorine-containing substances. 19F-Fluorine ventilation and perfusion studies]. *Fortschr Geb Rontgenstr Nuklearmed*. 1984;140(3):239–243.

108. Kuethe DO, Caprihan A, Fukushima E, Waggoner RA. Imaging lungs using inert fluorinated gases. *Magn Reson Med*. 1998;39(1):85–88.

109. Couch MJ, Ball IK, Li T, et al. Pulmonary ultrashort echo time 19F MR imaging with inhaled fluorinated gas mixtures in healthy volunteers: feasibility. *Radiology*. 2013;269(3):903–909.

110. Halaweish AF, Michael Foster W, Moon RE, et al. Dynamics of pulmonary ventilation distribution at steady state via 19F fluorine-enhanced MRI: initial experiences and future developments. *International Society for Magnetic Resonance Imaging Proceedings*. Salt Lake, Utah USA; 2013.

111. Kuethe DO, Caprihan A, Gach HM, Lowe IJ, Fukushima E. Imaging obstructed ventilation with NMR using inert fluorinated gases. *J Appl Physiol (1985)*. 2000;88(6):2279–2286.

112. Carrero-Gonzalez L, Kaulisch T, Stiller D. In vivo diffusion-weighted MRI using perfluorinated gases: ADC comparison between healthy and elastase-treated rat lungs. *Magn Reson Med*. 2013;70(6):1761–1764.

113. Chang YV, Conradi MS. Relaxation and diffusion of perfluorocarbon gas mixtures with oxygen for lung MRI. *J Magn Reson*. 2006;181(2):191–198.

114. Couch MJ, Ball IK, Li T, et al. Inert fluorinated gas MRI: a new pulmonary imaging modality. *NMR Biomed*. 2014;27(12):1525–1534.

115. Jacob RE, Chang YV, Choong CK, et al. ¹⁹F MR Imaging of ventilation and diffusion in excised lungs. *Magn Reson Med*. 2005;54(3):577–585.

116. Pérez-Sánchez JM, Pérez de Alejo R, Rodríguez I, Cortijo M, Peces-Barba G, Ruiz-Cabello J. In vivo diffusion weighted 19F MRI using SF6. *Magn Reson Med*. 2005;54(2):460–463.

117. Ruiz-Cabello J, Pérez-Sánchez JM, Pérez de Alejo R, et al. Diffusion-weighted 19F-MRI of lung periphery: influence of pressure and air-SF6 composition on apparent diffusion coefficients. *Respir Physiol Neurobiol*. 2005; 148(1–2):43–56.

118. Edelman RR, Hatabu H, Tadamura E, Li W, Prasad PV. Noninvasive assessment of regional ventilation in the human lung using oxygen-enhanced magnetic resonance imaging. *Nat Med*. 1996;2(11):1236–1239.

119. Bauman G, Puderbach M, Deimling M, et al. Non-contrast-enhanced perfusion and ventilation assessment of the human lung by means of Fourier decomposition in proton MRI. *Magn Reson Med*. 2009;62(3):656–664.

120. Johnson KM, Fain SB, Schiebler ML, Nagle S. Optimized 3D ultrashort echo time pulmonary MRI. *Magn Reson Med*. 2013;70(5):1241–1250.

121. Möller HE, Chen XJ, Saam B, et al. MRI of the lungs using hyperpolarized noble gases. *Magn Reson Med*. 2002;47(6):1029–1051.

122. Couch MJ, Blasiak B, Tomanek B, et al. Hyperpolarized and inert gas MRI: the future. *Mol Imaging Biol*. 2015;17(2):149–162.

123. Kruger SJ, Nagle SK, Couch MJ, Ohno Y, Albert M, Fain SB. Functional imaging of the lungs with gas agents. *J Magn Reson Imaging*. 2016;43(2):295–315.

124. Ouriadov AV, Fox MS, Couch MJ, Li T, Ball IK, Albert MS. In vivo regional ventilation mapping using fluorinated gas MRI with an X-centric FGRE method. *Magn Reson Med*. 2015;74(2):550–557.

125. Parra-Robles J, Cross AR, Santyr GE. Theoretical signal-to-noise ratio and spatial resolution dependence on the magnetic field strength for hyperpolarized noble gas magnetic resonance imaging of human lungs. *Med Phys*. 2005;32(1): 221–229.

126. Halaweish AF, Charles HC. Physiorack: an integrated MRI safe/conditional, gas delivery, respiratory gating, and subject monitoring solution for structural and functional assessments of pulmonary function. *J Magn Reson Imaging*. 2014; 39(3):735–741.

127. De Zanche N, Chhina N, Teh K, Randell C, Pruessmann KP, Wild JM. Asymmetric quadrature split birdcage coil for hyperpolarized 3He lung MRI at 1.5T. *Magn Reson Med*. 2008;60(2):431–438.

128. Ouriadov A, Farag A, Kirby M, McCormack DG, Parraga G, Santyr GE, Pulmonary hyperpolarized (129) Xe morphometry for mapping xenon gas concentrations and alveolar oxygen partial pressure: proof-of-concept demonstration in healthy and COPD subjects. *Magn Reson Med*. 2015;74(6):1726–1732.

129. Farag A, Peterson JC, Szekeres T, et al. Unshielded asymmetric transmit-only and endorectal receive-only radiofrequency coil for (23) Na MRI of the prostate at 3 tesla. *J Magn Reson Imaging*. 2015;42(2):436–445.

130. Halaweish AF, Moon RE, Foster WM, et al. Perfluoropropane gas as a magnetic resonance lung imaging contrast agent in humans. *Chest*. 2013;144(4):1300–1310.

131. Couch MJ, Ball IK, Li T, et al. Optimized Strategies for ¹⁹F MRI of Human Lungs and Comparison of UTE and Gradient Echo Imaging. *Proc Intl Soc Mag Reson Med*. 2014:22.

132. Wolf U, Scholz A, Heussel CP, Markstaller K, Schreiber WG. Subsecond fluorine-19 MRI of the lung. *Magn Reson Med*. 2006;55(4):948–951.

133. Schreiber WG, Eberle B, Laukemper-Ostendorf S, et al. Dynamic (19)F-MRI of pulmonary ventilation using sulfur hexafluoride (SF(6)) gas. *Magn Reson Med*. 2001;45(4):605–613.

134. Kuethe DO, Behr VC, Begay S. Volume of rat lungs measured throughout the respiratory cycle using 19F NMR of the inert gas SF6. *Magn Reson Med*. 2002; 48(3):547–549.

135. Conradi MS, Saam BT, Yablonskiy DA, Woods JC. Hyperpolarized 3He and perfluorocarbon gas diffusion MRI of lungs. *Prog Nucl Magn Reson Spectrosc*. 2006;48(1):63–83.

136. Adolphi NL, Kuethe DO. Quantitative mapping of ventilation-perfusion ratios in lungs by 19F MR imaging of T1 of inert fluorinated gases. *Magn Reson Med*. 2008;59(4):739–746.

137. Couch MJ, Ouriadov A, Santyr GE. Regional ventilation mapping of the rat lung using hyperpolarized (1)(2)(9)Xe magnetic resonance imaging. *Magn Reson Med*. 2012;68(5):1623–1631.

138. Deninger AJ, Månsson S, Petersson JS, et al. Quantitative measurement of regional lung ventilation using 3He MRI. *Magn Reson Med*. 2002;48(2):223–232.